

Hull form optimization based on calm-water wave drag with or without generating bulbous bow

Xinwang Liu^a, Weiwen Zhao^a, Decheng Wan^{a,b,*}

^a Computational Marine Hydrodynamics Lab (CMHL), School of Naval Architecture, Ocean and Civil Engineering, Shanghai Jiao Tong University, Shanghai 200240, China

^b Ocean College, Zhejiang University, Zhoushan 316021, China

ARTICLE INFO

Keywords:

Wave drag
Hull form optimization
NURBS
Bulbous bow generation
OPTShip-SJTU

ABSTRACT

In the ship design process, hull form design and optimization play an important role. In the research and engineering fields of hull form optimization, the resistance performance is most noticed among all the hydrodynamic performances. In this paper, we focus on the calm-water drag optimization for a high-speed slender hull without a bulbous bow, and the generation of the bulbous bow is introduced in detail, such as the hull form deformation methods and the knot-insertion procedure for the NURBS surface. Two optimization cases are given. In case 1, only shifting method is used, while in case 2, shifting and Radial Basis Function (RBF) methods are both used. During the hydrodynamic evaluation of the new sample hulls, the potential flow solver is applied, and the verification and validation procedure is done at first. The genetic algorithm is used to obtain two optimal ships with minimum wave drag. Optimization results show that even when we do not generate a bulbous bow, the optimal hull will have a relatively big decrease of the wave drag coefficient. However, favorable interference of the wave systems conducted by the generated bulbous bow can help reduce the wave drag coefficient to a greater extent, showing that the bulbous bow generation method proposed in this paper has potentials in the resistance optimization of the medium- or high-speed ship hulls.

1. Introduction

In the process of ship design, hull form design is vital, which has attracted the attention of a large number of researchers and ship designers. In order to obtain a modified ship with better hydrodynamic performances, the initial hull should be optimized. In recent years, with the enormous development of computer technology and calculation theories, the Simulation-Based-Design (SBD) approach is becoming possible rather than empirical formulas or the experience of designers. It is a new design way which integrates hull form modification, numerical simulations and optimization technology.

Scholars at home and abroad have done a series of researches on hull form optimization problems, and achieved good results. Tahara et al. (2008) introduced six design variables to control the shape of hull lines, and optimized the bow, sonar and stern lines of DTMB-5415 through parametric model method. Peri et al. (2001) regarded the total resistance and the bow wave amplitude as the objective functions of the geometry of a tanker bulbous bow, and used three different optimization algorithms including Conjugate Gradient (CG), Sequence Quadratic

Programming (SQP), and Steepest Descent (SD) methods to do the optimizations, and the optimization results were finally verified by the model test. Campana et al. (2006) used the Non-Uniform Rational B-Spline (NURBS) surface modeling method to modify a bulbous bow, and the modified hulls were evaluated by RANS-based solver, indicating the bulbous was optimized. Kim et al. (2011) took the total resistance as the objective function and the Multi-Objective Genetic Algorithm (MOGA) as the optimization algorithm to optimize the resistance performance of the Series 60 ship at three speeds, where the shifting and Radial Basis Function (RBF) methods were used to modify the ship hull. Diez et al. (2015) applied Karhunen-loève expansion to reduce the dimensionality of the design space of Free-Form Deformation (FFD) method in order to save computer costs. Li et al. (2013) used the Multi-Objective Particle Swarm Optimization (MOPSO) algorithm and FFD method to optimize the stern shape of a 6600DWT bulk carrier, whose resistance was reduced significantly. Zhang et al. (2009) used Rankine source method to calculate the wave-making resistance and Non-Linear Programming (NLP) as the optimization algorithm to get the optimal hull form with minimum wave-making resistance. Peri (2016)

* Corresponding author.

E-mail address: dcwan@sjtu.edu.cn (D. Wan).

<https://doi.org/10.1016/j.apor.2021.102861>

Received 10 April 2021; Received in revised form 8 August 2021; Accepted 28 August 2021

Available online 9 September 2021

0141-1187/© 2021 Elsevier Ltd. All rights reserved.

came up with a method to do the robust optimization of a bulk carrier in order to minimize the expectation and the standard deviation of the unit transportation cost using Particle Swarm Optimization (PSO) algorithm. Wu et al. (2017) used FFD method to change the bulbous bow shape of DTMB-5415 in order to obtain optimal hulls with better resistance performances in different speeds. Tezdogan et al. (2018) used a hybrid algorithm to optimize the total resistance in calm water of a fishing boat, where two optimal hulls were obtained by two schemes. Yang and Huang, 2016 used surrogate models to perform three optimization cases that were validated by cross validation, where each sample point was evaluated from the surrogate model constructed by the rest of the sample points.

As mentioned above, researchers have focused on the hull form modification, hydrodynamic evaluation, surrogate model construction, and optimization algorithms in the field of hull form optimization. Therefore, a self-developed optimization tool integrating the modules above is essential for us to do the SBD automatically.

For the resistance evaluation, there are mainly two kinds of methods to calculate the resistance of the hull. One is based on the potential flow theory which is widely used to calculate the wave-making resistance of the slender hull, especially for the hulls sailing in relatively high speeds. The main advantage of this method is that it can calculate the wave-making resistance in a few minutes and has relatively high fidelity which can be applied in the preliminary design stage. The other is based on Computational Fluid Dynamics (CFD) considering viscosity. Although CFD has developed rapidly in recent years, the methods based on potential flow theory still have their future. The main reason is that in the ship preliminary design stage, designers need to quickly and accurately evaluate the resistance performance of the hull forms in order to do hull form design or optimization.

One of the potential-flow-based methods is Neumann-Michell theory (NM theory) (Noblesse et al., 2013), based on the Neumann-Kelvin theory (NK theory). NM theory eliminates the ship waterline integral item in the NK theory, and the whole calculation can be converted to the integral on the wet surface of the ship. The theory adopts the consistent linear flow model and there's no need to solve the distribution on the boundary of the source but calculate the wave resistance through the iteration of velocity potential. Besides, there are a lot of researches about comparisons of experimental measurements of wave drag with numerical predictions obtained using the NM theory for the Wigley hull, the Series 60 and DTMB-5415 model. Zhang et al. (2015) used self-developed the NMShip-SJTU solver based on NM theory and calculated the resistance of catamaran, including the Delft catamaran and Series 60 catamaran in different demihull spacings. The results showed that the calculation results are in good agreement with experimental measurements. Liu and Wan (2017) simulated the wave interference caused by the horizontal and the longitudinal demihull spacings of the quadramarans using NM theory. Yang et al. (2013) presented that the sum of the ITTC friction resistance and the NM theory wave resistance could be expected to yield realistic practical estimates, which could be useful for routine applications to design and ship hull form optimization of a broad range of displacement ships. The computation of the steady flow around a moving ship based on NM theory is efficient and robust due to the succinctness of this theory, and Kim et al. (2009) has already pointed that the wave resistance predicted by NM theory is in fairly good agreement with experimental measurements. To sum up, using NM theory can quickly complete the resistance performance forecast on personal computers.

Calculating the resistance of the ship based on CFD considering viscosity, by contrast, takes more time. However, for further investigation with high fidelity, the CFD method can be used to do the verification of the hulls and even the optimization. The naoe-FOAM-SJTU solver (Shen et al., 2012; Wang et al., 2019), developed on open source platform OpenFOAM (2016), has been extensively validated on a great many ship hydrodynamic cases, such as ship resistance (Zha et al., 2014), seakeeping (Shen and Wan, 2013; Zhuang and Wan, 2021),

propulsion (Zhao et al., 2020a) and maneuvering (Zhang et al., 2020; Zhao et al., 2020b), showing that the naoe-FOAM-SJTU solver can deal well with the hydrodynamic evaluations of the ships.

In this paper, we mainly focus on the calm-water drag optimization for a high-speed slender hull without a bulbous bow. Even when we do not generate a bulbous bow, the optimal hull will have a relatively big decrease of the wave drag coefficient. However, favorable interference of the wave systems conducted by the generated bulbous bow can help reduce the wave drag coefficient to a greater extent. Therefore, the generation of the bulbous bow is introduced in detail, such as the choice of hull form deformation methods and the knot-insertion procedure for the NURBS surface, and the two optimization cases are given for comparing the optimization effect with or without generating a bulbous bow. Furthermore, although the potential flow solver is used by some articles for drag evaluation or even optimization, rare articles did the verification and validation, so the procedure is done as a reference here. Last but not the least, the way in which constraints are handled deserves a deep discussion especially for the hull form optimization problems. Actually, there are several levels/methods to apply constraint conditions in hull form optimization designs, being discussed here, which were seldom mentioned in the existing studies in hull form optimization field.

2. Optimization solver OPTShip-SJTU

The whole optimization process is implemented using the in-house solver OPTShip-SJTU, which is based on C++ language for the ship hull form optimization. The solver integrates with a hull form modification module, a hydrodynamic performance evaluation module, a surrogate model construction module and an optimization module, which can achieve the ship hull form optimization design automatically. The structure of the OPTShip-SJTU solver is shown in Fig. 1 and the modules will be introduced in detail in the following optimization applications.

2.1. Hull form modification

Hull form modification module plays a major role in the entire optimization process. Traditionally, a new series of variables are selected during the design of experiment, and the hull form modification module needs to make rapid response to the certain set of optimization design variables, that is, to generate meshes of the new ship hulls, and send them to the ship hydrodynamic performance evaluation module, then the evaluation results will further affect the optimization module to find the optimal ship hull.

In order to generate new hulls, there are mainly two kinds of hull form representation types. One is the discrete mesh, for example, by the STereoLithography (STL) file. The discrete mesh of the hull can be directly deformed by changing the coordinates of each mesh point using different deformation methods such as shifting method, Free-Form Deformation method, and Radial Basis Function method.

Free Form Deformation (FFD) method was first proposed by Sederberg and Parry (1986), which is chosen to perform the deformation of solid geometric models, and has been widely used in various fields including hull geometry reconstruction and other transportation tools. The main idea can be seen in author's previous article (Liu et al., 2018).

By changing the moving number, direction and distance of the moveable control points after determining the control lattice(s), different new hull meshes can be obtained. For instance, the hull bulbous bow can be modified by FFD method which is shown below in Fig. 2, where the lower left is the initial bulbous bow and the lower right is the modified bulbous bow.

For the shifting method (Yang and Huang, 2016), modified function g is introduced to modify the Section Area Curve (SAC) of ship hull and new hull forms can be obtained by shifting hull lines of each station along the x direction:

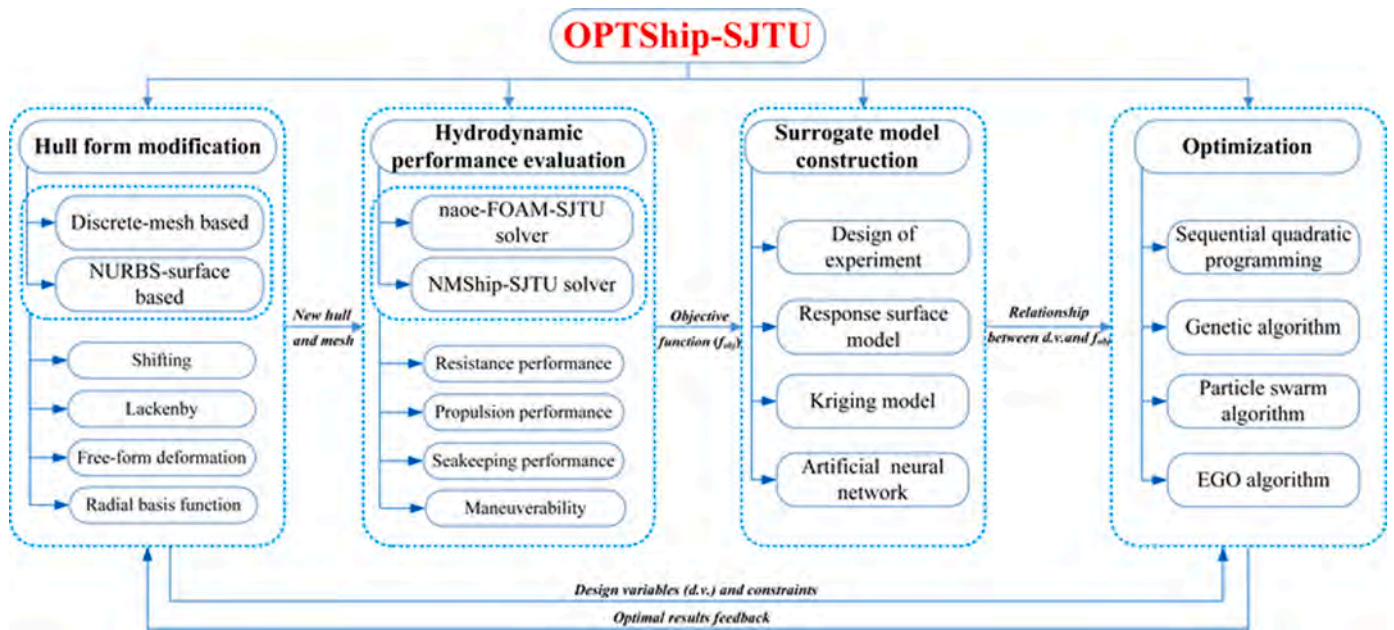


Fig. 1. Framework diagram of OPTShip-SJTU.

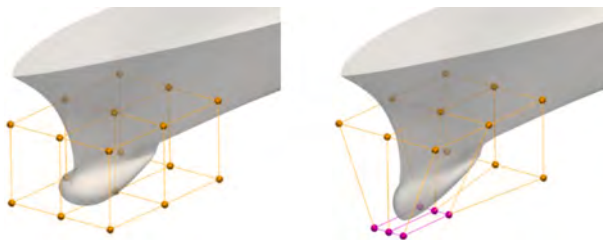


Fig. 2. Bulbous bow modification through FFD method.

$$g = \begin{cases} \alpha_1 \left[0.5 \left(1 - \cos 2\pi \frac{x - \alpha_2}{\alpha_2 - x_1} \right) \right]^{0.5}, & x_1 \leq x < \alpha_2 \\ -\alpha_1 \left[0.5 \left(1 - \cos 2\pi \frac{x - \alpha_2}{\alpha_2 - x_2} \right) \right]^{0.5}, & \alpha_2 \leq x \leq x_2 \\ 0, & \text{elsewhere} \end{cases} \quad (1)$$

where x_1, x_2 represents the start and end points of the shifting range in x direction, α_1 represents the amplitude of the modified function, and α_2 represents the fixed point (section) in the shifting range. The SAC of the initial hull and the deformed hull is shown by the black dot line and green solid line in Fig. 3.

For instance, the Wigley hull with the waterline length of 1 m can be modified by shifting method which is shown below, where Fig. 4 is the comparison of body plans between the original and a sample deformed hull, Fig. 5 is the comparison of sheer plans between the original and the sample deformed hull, and Fig. 6 is the comparison of SACs between the original and the sample deformed hull named “model1”.

The Radial Basis Function (RBF) method (Wendland, 1995) is a scalar function symmetric along the radial direction. The interpolation function can be approximated by a sum of the radial basis functions and a polynomial as follows:

$$s(\mathbf{X}) = \sum_{j=1}^N \lambda_j \phi(\|\mathbf{X} - \mathbf{X}_j\|) + p(\mathbf{X}) \quad (2)$$

where (x_j, y_j, z_j) is the coordinates of the RBF control point \mathbf{X}_j , $s(\mathbf{X})$ is the

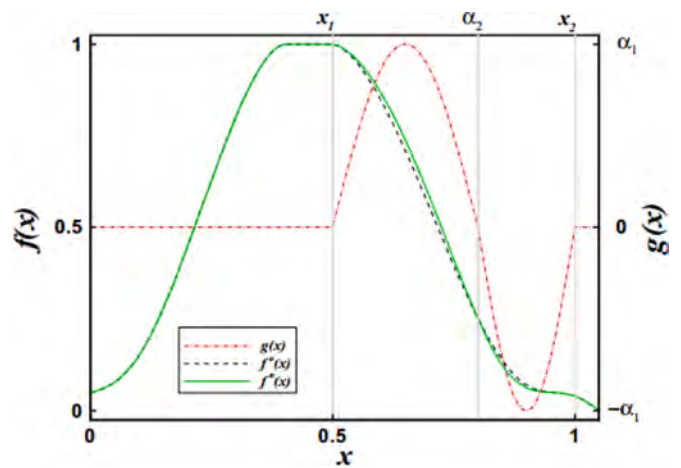


Fig. 3. SAC comparison of the original and deformed hulls.

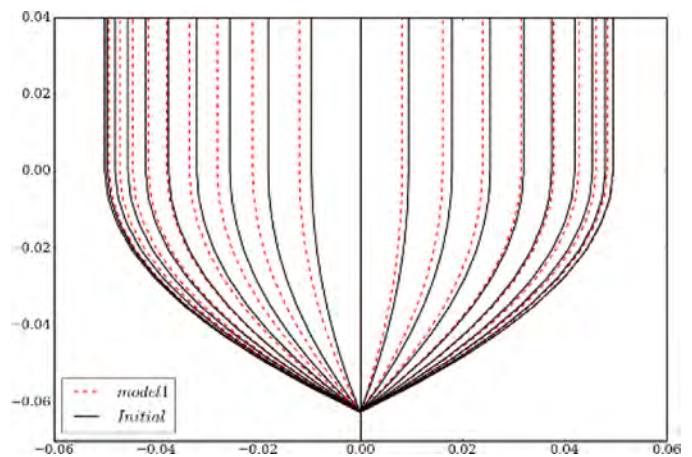


Fig. 4. Comparison of body plans between the two hulls.

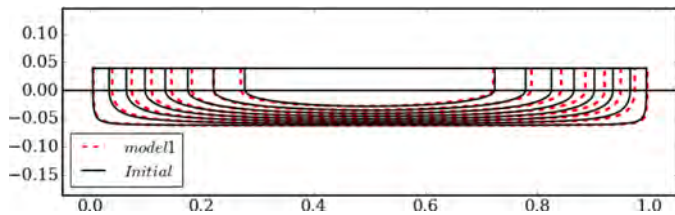


Fig. 5. Comparison of sheer plans between the two hulls.

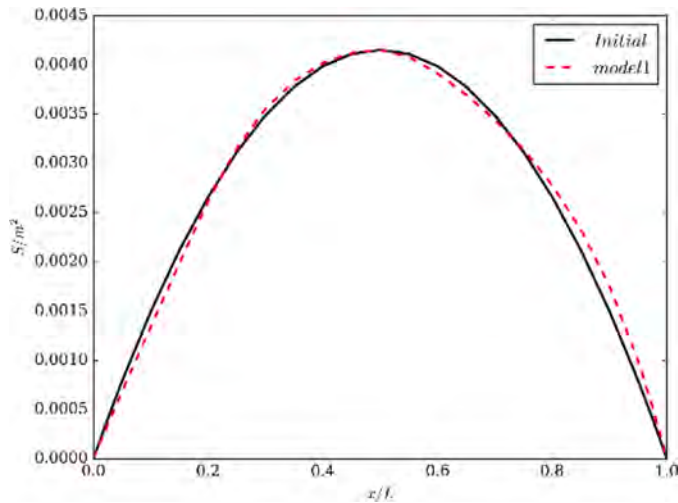


Fig. 6. Comparison of SACs between the two hulls.

displacement of every control point $\mathbf{X}(x, y, z)$, N is the number of RBF moving and fixed control points, and ϕ is a given radial basis function with respect to the Euclidian norm (distance) $\|\cdot\|_2$.

The low-order polynomial $p(\mathbf{X})$ represents the affine transformation:

$$p(\mathbf{X}) = c_1 + c_2x + c_3y + c_4z \quad (3)$$

What's more, ϕ represents the radial basis function, which has many optional forms. We choose the compact support radial basis function Wendland (1995) $\psi_{3,1}$ as ϕ :

$$\phi(\|\mathbf{X}\|) = \begin{cases} (1 - \|\mathbf{X}\|/r)^4(4\|\mathbf{X}\|/r + 1), & 0 \leq \|\mathbf{X}\| \leq r \\ 0, & \|\mathbf{X}\| > r \end{cases} \quad (4)$$

where r is the support radius, that is, when the distance of point \mathbf{X} and \mathbf{X}_j is bigger than r , the moving of \mathbf{X}_j does not have any influence on \mathbf{X} ; Otherwise, the point \mathbf{X} will have a new location related to point \mathbf{X}_j , and the smaller distance, the greater influence.

In order to determine the coefficients $\lambda_j (j = 1, 2, \dots, N)$ and $c_k (k = 1, 2, 3, 4)$ in Eq. (2), we have the interpolation conditions:

$$s(\mathbf{X}_j) = f_j, j = 1, 2, \dots, N \quad (5)$$

where each f_j is a known value which is the given displacement on a moving or fixed RBF control point. We also have the additional conditions to determine c_k :

$$\sum_{j=1}^N \lambda_j p(\mathbf{X}_j) = 0, j = 1, 2, \dots, N \quad (6)$$

As a result, the linear equations of λ_j, c_k can be obtained:

$$\begin{pmatrix} \mathbf{M} & \mathbf{q} \\ \mathbf{q}^T & \mathbf{0} \end{pmatrix} \begin{pmatrix} \boldsymbol{\lambda} \\ \mathbf{c} \end{pmatrix} = \begin{pmatrix} \mathbf{f} \\ \mathbf{0} \end{pmatrix} \quad (7)$$

where vectors $\boldsymbol{\lambda} = [\lambda_1, \lambda_2, \dots, \lambda_N]^T$, $\mathbf{c} = [c_1, c_2, c_3, c_4]^T$, $\mathbf{f} = [f_1, f_2, \dots, f_N]^T$,

$$\text{and matrixes } M_{ij} = \phi(\|\mathbf{X}_i - \mathbf{X}_j\|), i, j = 1, 2, \dots, N, \mathbf{q} = \begin{bmatrix} 1 & x_1 & y_1 & z_1 \\ 1 & x_2 & y_2 & z_2 \\ \vdots & \vdots & \vdots & \vdots \\ 1 & x_n & y_n & z_n \end{bmatrix}.$$

All points on or near the ship hull surface are divided into three types:

- (a) Fixed control points;
- (b) Movable control points;
- (c) Dependent points (whose displacements depend on the movable control points).

It should be noted that, apart from directly deforming the hull mesh, the hull surface (NURBS surface) can also be deformed, such as by the Initial Graphics Exchange Specification (IGES) file, because the hull surface is usually defined by Non-Uniform Rational B-Splines (NURBS) in the IGES file. By changing the control points or weight factors of the NURBS surfaces, the new hull's IGES file can be obtained, and further transformed to the discrete mesh file in order to do the hydrodynamic evaluations. The NURBS surface of the hull can also be deformed using different deformation methods mentioned above.

For the initial Wigley hull, the yellow surface represents the NURBS surface and the red points represent the control points of the NURBS surface shown below in Fig. 7.

After the coefficients λ_j, c_k are obtained, the displacement of all the NURBS control points of the hull can be evaluated using Eq. (2), thus the new points of the new hull surface can be got.

2.2. Hydrodynamic performance evaluation

For the hydrodynamic evaluation in this paper, considering that the sailing speed Froude number Fr is relatively high and the objective function is the wave-making drag coefficient, a potential-flow-based solver is used to calculate the wave-making drag coefficient of the new hulls.

The Neumann-Michell theory is the improvement of the Neumann-Kelvin (NK) theory based on a consistent linear potential flow model.

The flow about the ship can be observed from a righthanded moving system of orthogonal coordinates $\mathbf{X} \equiv (X, Y, Z)$ attached to the ship (the X axis is chosen along the path of the ship and points toward the ship bow; the Y axis is parallel to the mean free surface and points toward the right side of the ship; and the Z axis is vertical and points upward, with the mean free surface taken as the plane $Z = 0$, as shown in Fig. 8, and thus appears steady flow velocity given by the sum of an apparent uniform current $(-V_s, 0, 0)$ opposing the ship speed V_s and the disturbance flow velocity $\mathbf{U} \equiv (U, V, W)$ due to the ship. The ship length L_s and speed V_s are used to define the following three non-dimensional coordinates $\mathbf{x} \equiv \mathbf{X}/L_s$, flow velocity $\mathbf{u} \equiv \mathbf{U}/V_s$, and flow potential $\phi \equiv \Phi/(V_s L_s)$. (Noblesse et al., 2013)

The flow potential at flow-field point $\tilde{\mathbf{x}} \equiv (\tilde{x}, \tilde{y}, \tilde{z})$ or boundary point $\mathbf{x} \equiv (x, y, z)$ is identified as $\tilde{\phi} = \phi(\tilde{\mathbf{x}})$ or $\phi = \phi(\mathbf{x})$ respectively. The flow velocities can be obtained by $\tilde{\mathbf{u}} \equiv (\tilde{u}, \tilde{v}, \tilde{w}) \equiv \nabla \tilde{\phi}$ and $\mathbf{u} = (u, v, w) = \nabla \phi$.

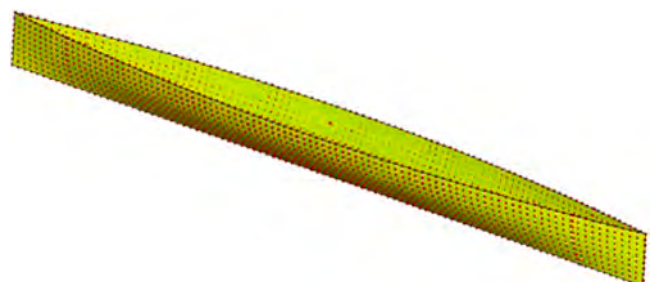


Fig. 7. NURBS surface and points for the Wigley hull.

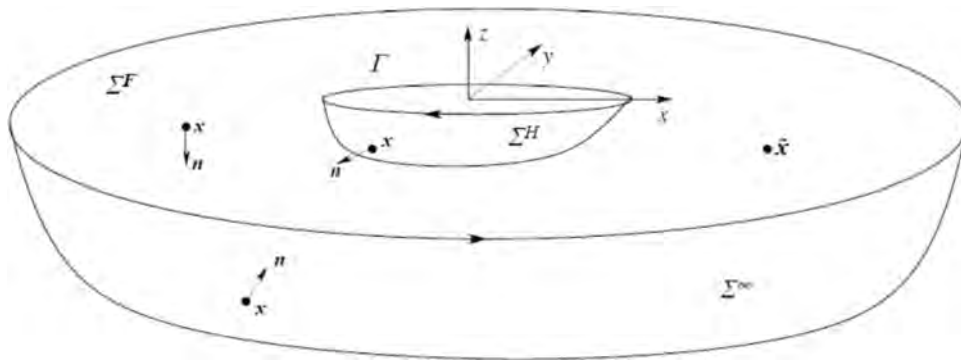


Fig. 8. Coordinate system and boundary sketch.

Furthermore, da denotes the differential element of area at a point \mathbf{x} of the ship hull surface Σ^H , and $\mathbf{n} = (n^x, n^y, n^z)$ is a unit vector that is normal to Σ^H at \mathbf{x} and points outside Σ^H , as shown in Fig. 8.

Green's function G is decomposed into the wave-making section W and the local flow section L ; the wave-making section W satisfies the radiation condition, the Kelvin-Michell linear free-surface boundary condition, and the Laplace equation. A wave function \mathbf{W} is introduced, and the wave-making section W and the wave function \mathbf{W} satisfy $\nabla \times \mathbf{W} = \nabla W$, and the wave function can be written as

$$\mathbf{W} = \left(0, W_z^x, -W_y^x \right) \quad (8)$$

where subscripts z and y stand for the first-order partial derivatives of W in z - and y -direction, respectively; superscript x represents the integral of x . Furthermore, π^G and π^ϕ are set to be the differential operators on G and ϕ , and they are respectively defined as

$$\begin{aligned} \pi^G &\equiv G_z + Fr^2 G_{xx} \\ \pi^\phi &\equiv \phi_z + Fr^2 \phi_{xx} \end{aligned} \quad (9)$$

where G_z is the first-order partial derivative of G with respect to z ; G_{xx} is the second-order partial derivative of G with respect to x ; ϕ_z is the first-order partial derivative of ϕ with respect to z ; ϕ_{xx} is the second-order partial derivative of ϕ with respect to x ; Fr is the Froude number of the hull.

By means of a series of mathematical transformations, the final simplified NM velocity potential can be expressed as

$$\tilde{\phi} \approx \tilde{\phi}_H + \tilde{\psi}^W \quad (10)$$

where

$$\tilde{\phi}_H = \int_{\Sigma^H} Gn^x da - \int_{\Sigma^F} G\pi^\phi dx dy \quad (11)$$

$$\tilde{\psi}^W = \int_{\Sigma^H} (-\phi_t \mathbf{d}' + \phi_{d'} \mathbf{t}') \cdot \mathbf{W} da \quad (12)$$

Here, \mathbf{t}' and \mathbf{d}' are two unit vectors tangent to the wetted surface of the hull, which are respectively taken as

$$\begin{aligned} \mathbf{t}' &= (v, -n^x v^y, n^y v^z) \\ \mathbf{d}' &= (0, -v^z, v^y) \\ v &= \sqrt{(n^y)^2 + (n^z)^2} \\ (v^y, v^z) &= (n^y, n^z)/v \end{aligned} \quad (13)$$

On the port side of the hull, the unit vector \mathbf{d}' points upward; on the starboard side of the hull, the unit vector \mathbf{d}' points downward. At an arbitrary position of the hull, the unit vector \mathbf{t}' always points to the bow, and \mathbf{t}' and \mathbf{d}' are always perpendicular to each other. ϕ_t and $\phi_{d'}$ stand for the \mathbf{t}' - and \mathbf{d}' -component of the velocity on the wetted surface of the hull.

After the calculation of the potential distribution $\tilde{\phi}$ on the ship hull surface, a series of hydrodynamic coefficients including wave-making

drag coefficient C_w , sinkage h and trim τ can be finally obtained.

NMShip-SJTU solver is self-developed according to the formulas above based on Neumann-Michell theory, and the input file contains the ship hull mesh, free surface mesh and ship main parameters, and we can get pressure distribution of the hull, wave-making drag of the hull, wave height along the hull and wave elevation of the free surface, etc.

The flowchart of NMShip-SJTU is shown below in Fig. 9.

Taking viscosity into consideration, the naoe-FOAM-SJTU solver is developed based on the open source platform OpenFOAM to solve typical hydrodynamic problems of ship and marine engineering. The solver mainly consists of a 6-DoF motion module, a mooring system module, a 3-D numerical wave tank module and a dynamic overset grid module. For the calm-water resistance calculation, the Reynolds-Averaged Navier-Stokes (RANS) equations are solved with the Pressure-Implicit with Splitting of Operations (PISO) loops for the whole unsteady turbulent flow field. A Volume-Of-Fluid (VOF) approach with bounded compression technique is used (Berberović et al., 2009) to capture the free surface. The $k-\omega$ Shear Stress Transport (SST) turbulence model (Menter et al., 2003) is employed to model the turbulence features. Furthermore, wall functions are used to model the velocity gradient effects near wall.

2.3. Surrogate model construction

As for the surrogate model construction module, in order to save computational costs, one alternative method is to construct a relatively simple surrogate model instead of complicated numerical analysis of a

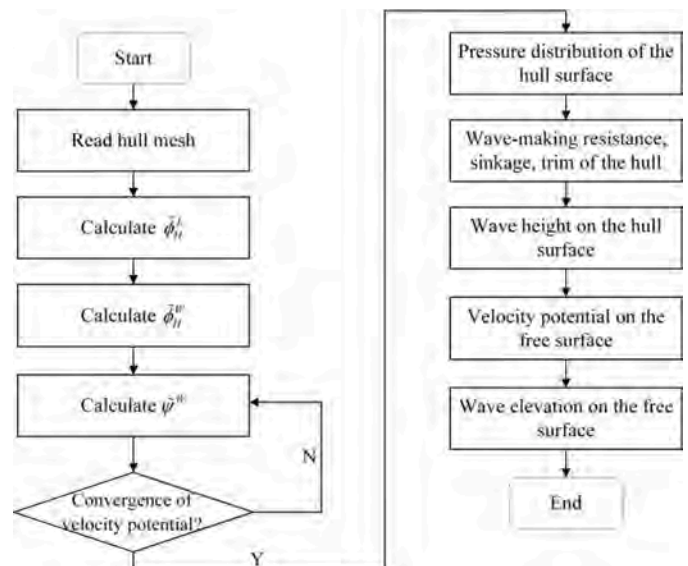


Fig. 9. flowchart of NMShip-SJTU.

large number of sample points in order to find the relationship, which is often with strong nonlinearity, between the design variables (input) and the objective functions (output). The sample points should be selected at the beginning of the optimization procedure, and the new meshes of them can be got, and then the hydrodynamic evaluation can be implemented.

The sample points can be selected using different design of experiment methods, for example, the Optimal Latin Hypercube Sampling (OLHS) method (Bates et al., 2004), and the Sobol method (Sobol, 1979).

After evaluating the hydrodynamic performances of the series of sample points, the surrogate model can be constructed. Some models are widely used such as Response Surface Model, Kriging model and Artificial Neural Network model. For instance, the Kriging surrogate model expresses the relationship between the design variables and the objective functions using a stochastic Gaussian process, which is able to exploit the spatial correlation of data in order to predict the shape of the objective function based only on limited information (Sykulski et al., 2011).

2.4. Optimization algorithm

To construct the surrogate model, we select 160 or 280 sample points in the design space by OLHS method in the following two optimization cases, and use the Kriging model to make quick evaluation in the optimization process. Finally, the Genetic Algorithm (GA) (Deb and Agrawal, 1995) is chosen as the optimization algorithm to solve the single-objective optimization problem. The quantities of iterations (generations) and population in each generation are 50 and 300 respectively for the genetic algorithm. Furthermore, the crossover fraction of genes swapped between individuals is set as 0.8, and the mutation rate is 0.2. Finally, the optimal hull forms in the two cases can be obtained with the termination criterion that the termination tolerances on fitness function value and constraints are both less than 10^{-6} .

3. Optimization case 1

3.1. Definition of the optimization problem

The optimization cases in this paper takes the Wigley hull as the initial ship, whose main dimensions can be seen in Table 1, and two views of the model can be seen in Fig. 10.

In the hull form optimization problem, the objective function is the minimum of the wave-making drag coefficient C_w shown in Eq. (14).

$$\min C_w = C_w(Fr=0.3) \quad (14)$$

3.2. Design variables

In the programming of the hull form deformation module, in order to deform the hull without the consideration of the different main dimensions of actual ship hulls, we first normalize the hull form with the waterline length 1, as shown in Fig. 8, and the boundary points' coordinates of the intersection of the water plane and the center longitudinal section are $(-0.5,0,0)$ and $(0.5,0,0)$. After obtaining the deformed hulls with the length 1, we can easily scale the hulls to the model scale in order to do the hydrodynamic calculations.

The optimization design variables (dimensionless) are used to change the shape of the hull. In this case, the shifting method is used in two regions (shown in Fig. 11) at the fore and aft parts of the hull.

Table 1
Main dimensions of Wigley hull.

Ship	Length/m	Width/m	Height/m
Wigley	4	0.4	0.25

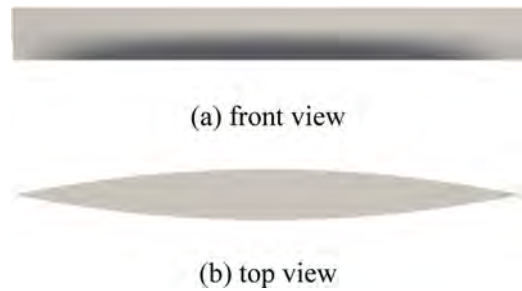


Fig. 10. Two views of Wigley hull.



Fig. 11. Two shifting regions of Wigley hull in case 1.

In shifting region 1, according to Eq. (1), the modified function g_1 can be written by setting $x_1 = 0, x_2 = 0.5$. Likewise, in shifting region 2, according to Eq. (1), the modified function g_2 can be written by setting $x_1 = -0.5, x_2 = 0$.

The OLHS method is firstly used to generate 160 sample points for 160 new hull forms which are uniformly distributed in the design space shown in Table 2, and calculate their wave-making resistance coefficient at $Fr = 0.3$.

3.3. Verification and validation of the potential-flow-based solver

Before using potential-flow-based or even viscous-flow-based solvers, ensuring their accuracy is vital. Combined with AIAA's CFD uncertainty procedure, Wilson et al. (2001) provided a comprehensive framework for the overall procedure of the CFD uncertainty method by giving an application for assessing RANS simulation of a container ship.

The uncertainty given by the researches above includes verification and validation. Verification is the procedure that evaluates whether the equations are solved right, while validation evaluates whether the right equations are solved.

Let the experimental data and numerical simulation result be denoted as D and S respectively. According to the NM theory, there's not the concept of time step and the iteration number δ_r can be set as 5×10^{-6} due to the convergence criterion of the velocity potential $\max_{x \in \Sigma^H} |\phi^{k+1} - \phi^k| < 10^{-5}$. Therefore, we mainly focus on the grid size δ_G by implementing (at least) 3 systematic solutions by refining grids with constant ratio r_G , that is

$$r_G = \frac{\Delta x_{G_2}}{\Delta x_{G_1}} = \frac{\Delta x_{G_3}}{\Delta x_{G_2}} = \dots = \frac{\Delta x_{G_N}}{\Delta x_{G_{(N-1)}}} \quad (15)$$

where N is the number of the solutions and Δx_{G_i} with $i = 1, 2, \dots, N$ ($i = 1$ for the finest) is the grid size of the i^{th} solution. As a rule, r_G is suggested to be $\sqrt{2}$.

For the verification procedure, the resistance coefficient difference of two adjacent grids is expressed as ϵ_G :

Table 2
Optimization design variables in case 1.

No.	Method	Region	Design Variables	Range
1	Shifting	Region 1 (fore part)	a_1	$[-0.02, 0.02]$
2			a_2	$[0.2, 0.3]$
3		Region 2 (aft part)	a_3	$[-0.02, 0.02]$
4			a_4	$[-0.3, -0.2]$

$$\varepsilon_{G21} = S_{G2} - S_{G1} \quad (16)$$

$$\varepsilon_{G32} = S_{G3} - S_{G2} \quad (17)$$

The convergence rate R_G is calculated as follows:

$$R_G = \frac{\varepsilon_{G21}}{\varepsilon_{G32}} \quad (18)$$

For 3 systematic solutions, a single estimate of the accuracy order and error calculated by the generalized Richardson extrapolation method can be provided.

Accuracy order estimation:

$$P_G = \frac{\ln(\varepsilon_{G32}/\varepsilon_{G21})}{\ln(r_G)} \quad (19)$$

Error estimation:

$$\delta_G^* = \frac{\varepsilon_{G21}}{r_G^{P_G} - 1} \quad (20)$$

The correction factor C_G can be calculated as follows, where $P_{Gest} = 2$, as recommended.

$$C_G = \frac{r_G^{P_G} - 1}{r_G^{P_{Gest}} - 1} \quad (21)$$

If the above C_G is taken as much less or more than 1 (lacking confidence), then the numerical (grid) uncertainty U_G is estimated:

$$U_G = |C_G \delta_G^*| + |(1 - C_G) \delta_G^*| \quad (22)$$

For the validation procedure, due to the lack of uncertainty of the original experiment, it is assumed that $U_D = 5\%D$, and the comparison error E is calculated as follows

$$E = D - S_{G1} \quad (23)$$

The calculation of validation uncertainty U_V can be obtained

$$U_V = \sqrt{U_G^2 + U_D^2} \quad (24)$$

In order to determine whether the validation is achieved or not, E and U_V are compared. If $|E| < U_V$, the combinations of all errors are less than U_V , and the validation is achieved at the level U_V . If $U_V \ll |E|$, the calculation model can be improved by E .

Although this CFD uncertainty procedure is still under discussion, a lot of numerical cases have already been evaluated through the overall procedure. However, it is rare to see the procedure implemented on the potential-theory based cases. Here, we try to use the procedure on our NMSHIP-SJTU solver in order to ensure the accuracy of the quick wave-making drag coefficient evaluation tool. More detailed equations in the verification and validation procedure can be seen in Wilson et al. (2001), and the results of the verification and validation parameters for $Fr = 0.289$ are shown in Table 3.

From Table 3, we can obtain that the calculation is monotonic convergent for three grids since the convergence rate R_G is between 0 and 1, and the numerical (grid) uncertainty is 1.376%. However, since the absolute value of real data D (experimental result) is too small, so the relative error E/D is still too large on the premise that the absolute error is small. In fact, it doesn't make much sense to just look at the relative error, but to look at the absolute error E . What's more, from the aspect of the changing trend of the calculated and measured C_t at different Froude numbers that will be given later, and the efficiency in comparing the drag performance of the deformed hulls, we can say that the NM solver can capture the drag change trend which can be used in the optimization process. The grids and dimensionless elevations of the free surface are shown below in Fig. 12. The grids and dimensionless pressure distributions of the hull are also shown in Fig. 13. From these two figures, we can see only little difference at the bow and stern parts of the hull.

Fig. 14 shows the comparison of the wave elevation calculated by

Table 3

Verification and validation parameters for NMSHIP-SJTU calculation for $Fr = 0.289$.

Grid	3	2	1
Hull panel grid dimensions ($N_x \times N_z$)	101 × 17	143 × 24	202 × 34
Free surface panel grid dimensions ($N_x \times N_y$)	651 × 100	930 × 143	1302 × 201
Total grid number	66,817	136,422	268,570
S_G (C_w)	1.505 × 10 ⁻³	1.516 × 10 ⁻³	1.524 × 10 ⁻³
ε_{G21}	-7.610 × 10 ⁻⁶		
ε_{G32}	-1.182 × 10 ⁻⁵		
R_G	0.644		
P_G	1.271		
δ_G^*	-1.376 × 10 ⁻⁵		
C_G	5.532 × 10 ⁻¹		
U_G	1.376 × 10 ⁻⁵		
D	1.0 × 10 ⁻³		
U_G/D	1.376%		
E	-0.524 × 10 ⁻³		
E/D	-52.4%		
U_V/D	5.186%		

NMSHIP-SJTU and naoe-FOAM-SJTU solvers. It is necessary to say that since the verification and validation of the naoe-FOAM-SJTU solver in the resistance calculation has already been given by Shen et al. (2012), it's not listed here. It can be seen that the amplitudes and the locations of the peaks and troughs of each wave system are almost the same, which can conclude that NMSHIP-SJTU solver can predict the wave elevation in calm water with relatively high fidelity.

Furthermore, experimental measurements given by the Ship Research Institute (SRI) and calculated results by the NMSHIP-SJTU solver of the wave-making resistance coefficient C_w , the frictional resistance coefficient C_f given by ITTC 1957 formula which can be written as Eq. (25), and the total resistance coefficient C_t which is simplified as the sum of C_w and C_f are shown in Fig. 15.

$$C_f = \frac{0.075}{(\lg Re - 2)^2} \quad (25)$$

It can be seen that the variation tendency between the experimental measurements and computational results of C_w with Fr increasing is almost the same, and the calculated C_t is quite close to the experimental C_t values, which shows that NMSHIP-SJTU solver is effective and efficient to do the hull form resistance optimization especially for the ships sailing in relatively high speeds.

Furthermore, the calculated wave height along the hull by NMSHIP-SJTU (NM) and naoe-FOAM-SJTU (CFD) is also compared with the experimental test result at $Fr = 0.289$ since there're no model test results for the flow field at $Fr = 0.30$, but their Froude number has just little difference.

From Fig. 16, it can be easily seen that not only the drag coefficient but also the flow field has relatively high fidelity.

The results above are also evidences for the validation since the NMSHIP-SJTU is not a viscous-flow solver to fit the experimental results to a nearly 100% extent.

3.4. Optimization results and analysis

After doing the hydrodynamic evaluations of the new hull forms, the Kriging surrogate model can be constructed. Through leave-one-out cross validation, we can see the accuracy of the constructed Kriging model in Fig. 17 and the mean square error is 1.139×10^{-13} .

Finally, we use genetic algorithm to get the optimization results. The convergence process of the best fitness can be seen in Fig. 18.

The initial and optimal hulls with their design variable values are shown in Table 4.

The hull lines comparisons are shown in Fig. 19. Totally speaking, we can see that the optimal hull is thinner than the initial one, and their free

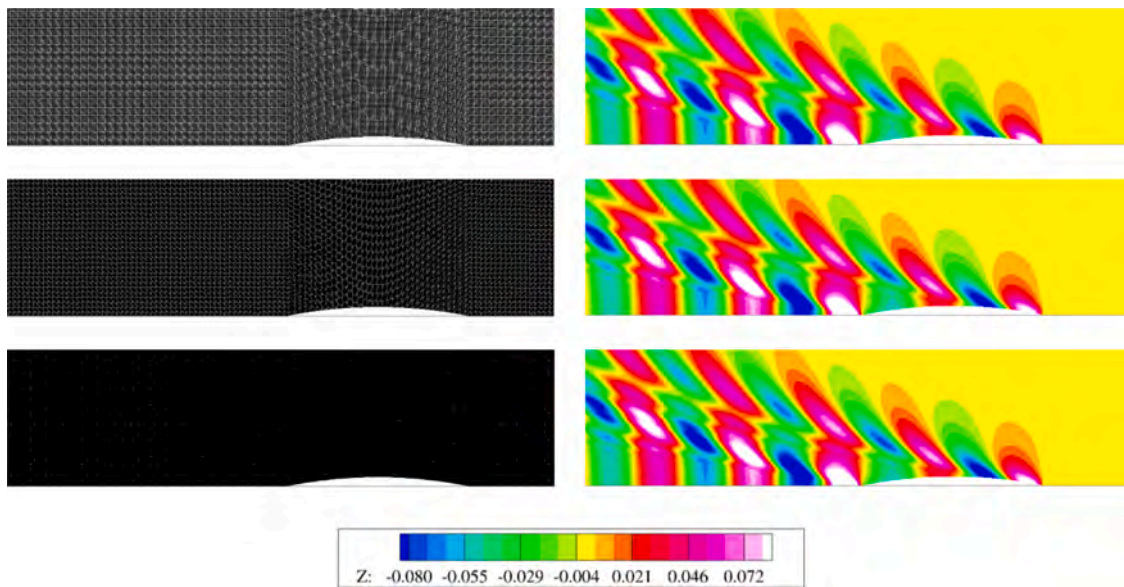


Fig. 12. Grids and dimensionless elevations of the free surface at $Fr = 0.289$.

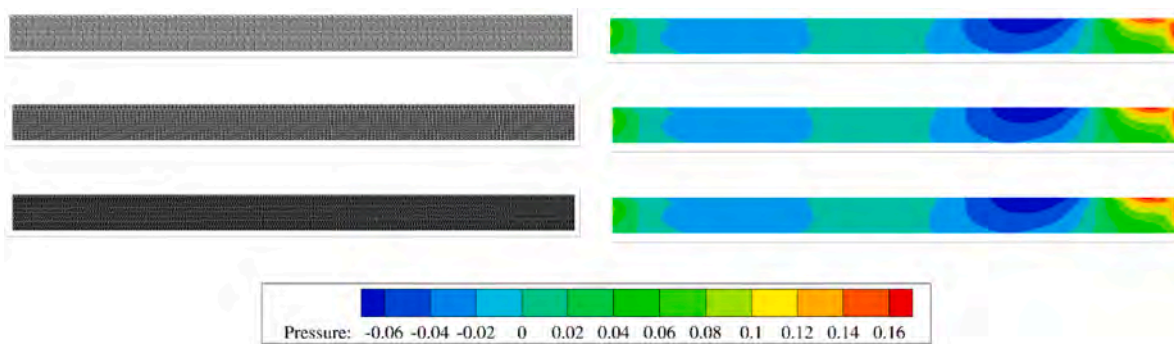


Fig. 13. Grids and dimensionless pressure distributions of the hull at $Fr = 0.289$.

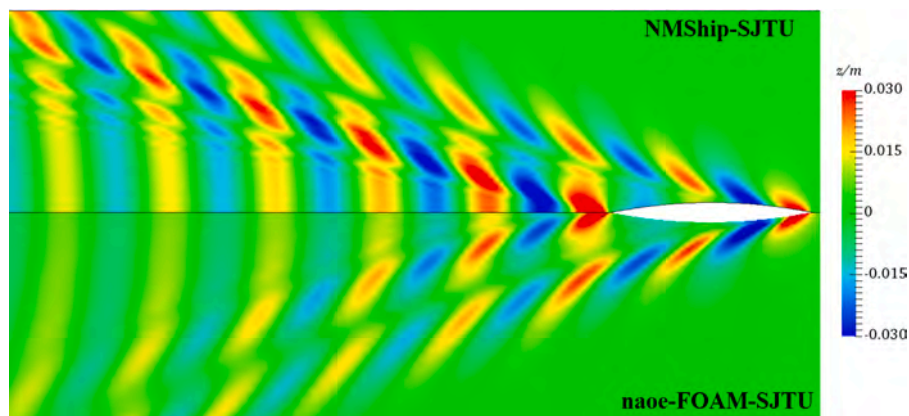


Fig. 14. Comparison of the wave elevation by two solvers at $Fr = 0.289$.

surface wave elevation comparison evaluated by NMShip-SJTU can be seen in Fig 20.

It can be easily observed that the peaks and troughs of bow and stern diverging waves, and the stern transverse wave are all decreased due to the shifting of the cross sections.

In order to do further verification, the calm-water resistances of the initial and optimal hulls are predicted by naoe-FOAM-SJTU, and their free surface wave elevation comparison evaluated by naoe-FOAM-SJTU

can be seen in Fig. 21.

Seen from Fig. 21, the peaks and troughs of bow and stern diverging waves, and the stern transverse wave are all decreased due to the shifting of the cross sections, and this decreasing trend is similar to that of the result given by NMShip-SJTU (shown in Fig. 20).

This not only ensure the reliability of the optimal hull, but also indicate the NMShip-SJTU solver can predict the wave drag (or the wave elevation) in calm water with relatively high fidelity.

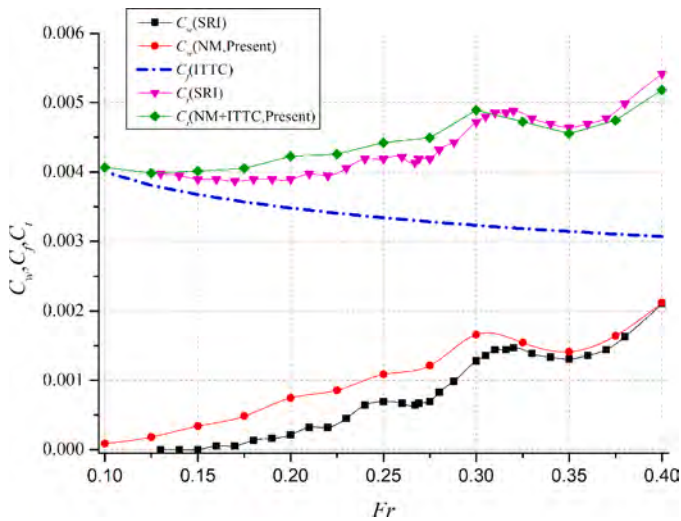


Fig. 15. Comparisons of the experimental and computational results of resistance coefficients.

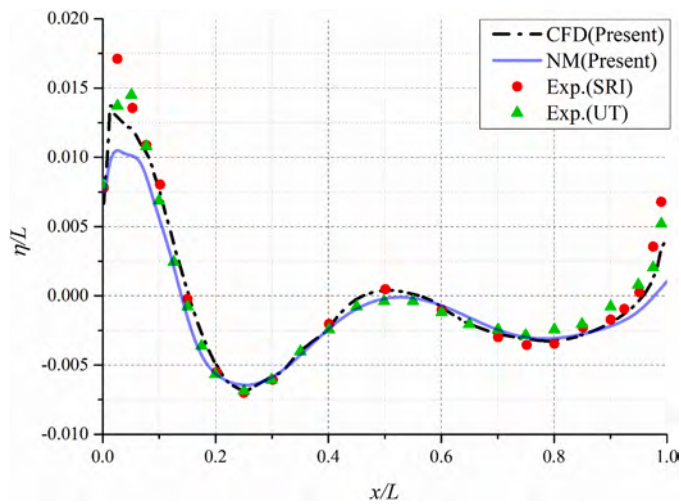


Fig. 16. Comparisons of the wave height along the hull at $Fr = 0.289$.

In fact, the calm-water total drag of the ship hull obtained from the RANS-based naoe-FOAM-SJTU solver is an integral component along the wet surface of the ship, which consists of two parts, namely, the frictional drag and the pressure drag, while the pressure drag consists of the viscous-pressure drag and the wave-making drag. However, the viscous-pressure drag and wave-making drag are difficult to separate. Here, the drag coefficients of the initial and optimal hulls calculated by the NM-based solver and RANS-based solver are listed in Table 5.

Seen from Table 5, for optimization case 1, the pressure drag coefficient C_p has a significant decrease, reaching 25.9%, which is close to the 25.3% decrease of the wave-making drag coefficient C_w obtained by the potential flow solver. Under the premise that the frictional drag coefficient C_f is almost unchanged, the total drag coefficient C_t also has a 9.2% decrease, indicating that for the high-speed slender ship, the total drag coefficient of the optimal hull obtained by the potential flow solver can also be reduced to some extent, indicating that the optimization results given above are reliable.

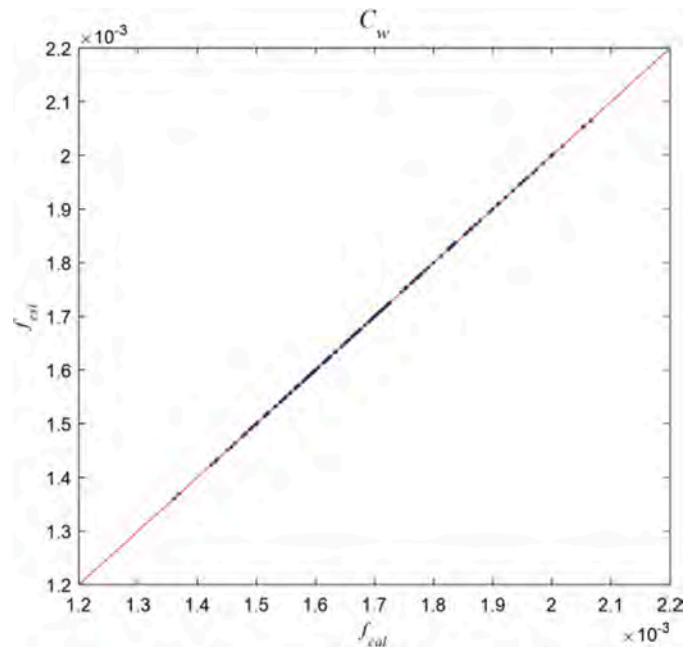


Fig. 17. Cross validation of Kriging surrogate model in case 1.

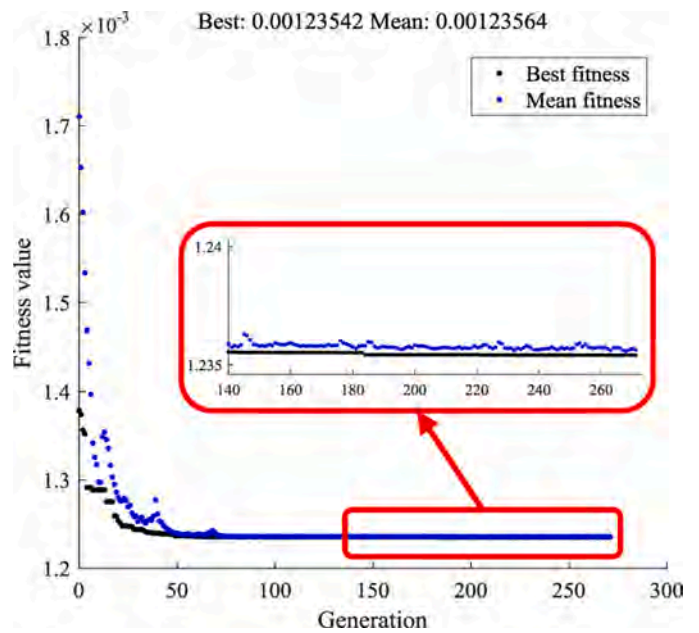


Fig. 18. Convergence of GA in case 1.

Table 4

Comparison of the design variables of initial and optimal hulls in case 1.

No.	Method	Design Variables	Initial Value	Optimal Value
1	Shifting	α_1	0	0.019
2		α_2	0	0.200
3		α_3	0	0.019
4		α_4	0	-0.200

4. Optimization case 2

4.1. Bulbous bow generation procedure

The main dimensions of the initial hull and objective function are the

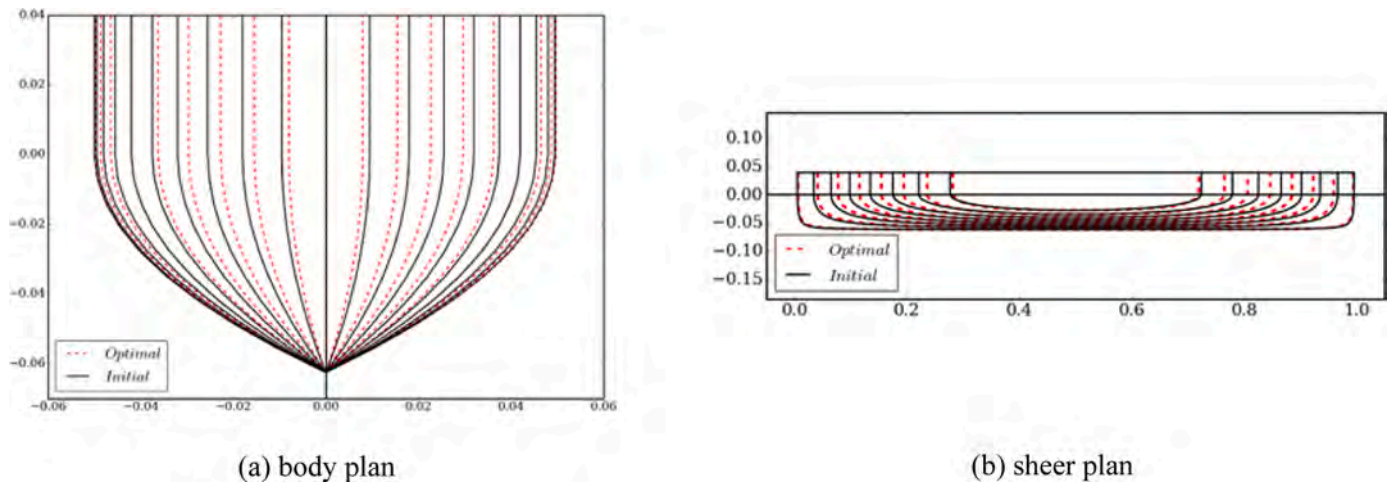


Fig. 19. Hull line comparisons of the two hulls in case 1 (Unit: m, with length 1).

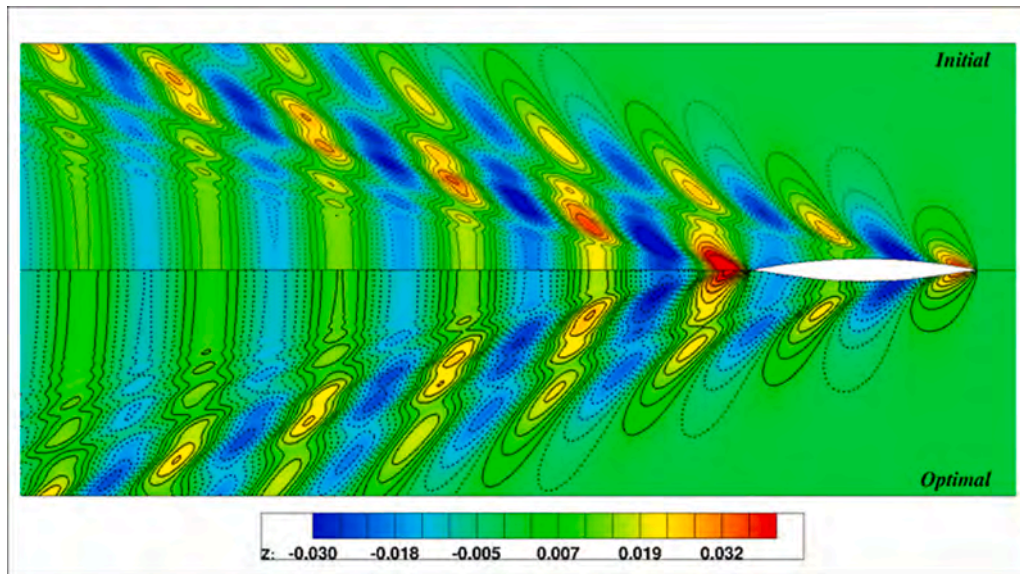


Fig. 20. Wave elevation comparisons of the two hulls in case 1 by NMSHIP-SJTU (Unit: m).

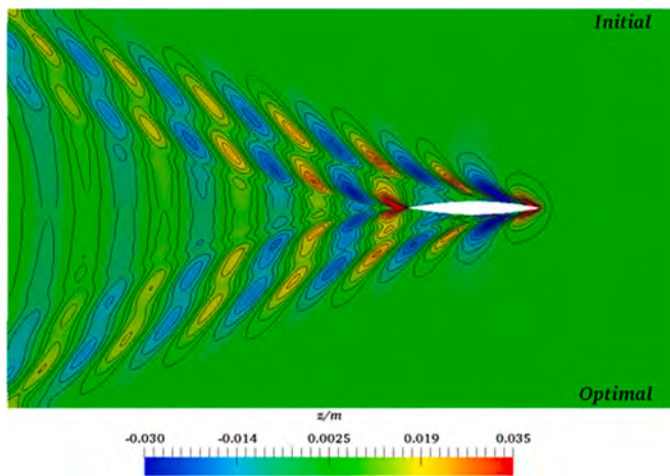


Fig. 21. Wave elevation comparisons of the two hulls in case 1 by naoe-FOAM-SJTU (Unit: m).

Table 5

Comparison of the drag coefficients of initial and optimal hulls in case 1.

	C_w (NM)	C_p (RANS)	C_f (RANS)	C_t (RANS)
Initial	1.66×10^{-3}	1.81×10^{-3}	2.87×10^{-3}	4.68×10^{-3}
Optimal	1.24×10^{-3}	1.34×10^{-3}	2.91×10^{-3}	4.25×10^{-3}
Decrease percent	25.3%	25.9%	-1.4%	9.2%

same with those in case 1.

Based on optimization case 1, we would like to further decrease the wave-making drag coefficient by generating a bulbous bow by using appropriate hull form deformation method.

As a matter of fact, we may face some problems when directly deforming the discrete mesh or NURBS surface:

At first, if we use the FFD method to generate a bulbous bow by directly deforming the discrete mesh, shown in Fig. 22, we can set two lattices and the two groups of red points are moving in x direction with different distances while the green ones are fixed in order to form a bulbous-like shape. The projections in the main view of the meshes are shown in Fig. 23, and it can be seen that a bigger bulbous bow may cause poorer quality of the new hull mesh. What's more, it is hard to control the outline of the bulbous bow.



Fig. 22. Two lattices for generating a bulbous bow by FFD method.

Therefore, we have tried to use the RBF method to generate a bulbous bow in order to easily control the outline of the bulbous bow by directly deforming the NURBS surface.

After selecting the fixed (green) and moveable (blue) control points of the Wigley hull, we can solve Eq. (7) in order to get the new locations of each point (pink) (shown in Fig. 24), and then the new surface can be obtained.

However, when we transform the new hull surface to the discrete mesh, when the control points are not refined (shown in Fig. 24), the mesh may be locally rough at the bow part (shown in Fig. 25) because the control points are relatively few at the bow if not refined.

As a result, in order to ensure the quality of the deformed mesh transformed by the new NURBS surface, we'd better do the local 'refinement' (knot insertion) of the NURBS control points at the bow part.

A p^{th} -degree in u direction and q^{th} -degree in v direction NURBS surface is defined as

$$S(u, v) = \frac{\sum_{i=0}^n \sum_{j=0}^m N_{i,p}(u) N_{j,q}(v) \omega_{i,j} P_{i,j}}{\sum_{i=0}^n \sum_{j=0}^m N_{i,p}(u) N_{j,q}(v) \omega_{i,j}}, a \leq u \leq b, c \leq v \leq d \quad (26)$$

where $P_{i,j}$ is the coordinate of the control points; $\omega_{i,j}$ is the weight of the control point $P_{i,j}$; u and v are the parametric knots corresponding to the control points $P_{i,j}$; $N_{i,p}(u)$, $N_{j,q}(v)$ are the B-spline basis functions of degree p and q in the u and v directions, given by

$$\begin{cases} N_{i,0}(u) = \begin{cases} 1, & \text{if } u_i \leq u \leq u_{i+1} \\ 0, & \text{else} \end{cases} \\ N_{i,p}(u) = \frac{u - u_i}{u_{i+p} - u_i} N_{i,p-1}(u) + \frac{u_{i+p+1} - u}{u_{i+p+1} - u_{i+1}} N_{i+1,p-1}(u) \\ 0 = 0 \end{cases} \quad (27)$$

Eq. (27) is based on the non-uniform knot vectors U and V , which are

$$U = \left\{ \underbrace{a, \dots, a}_{p+1}, u_{p+1}, \dots, u_{r-p-1}, \underbrace{b, \dots, b}_{p+1} \right\} \quad (28)$$

$$V = \left\{ \underbrace{c, \dots, c}_{q+1}, v_{q+1}, \dots, v_{s-q-1}, \underbrace{d, \dots, d}_{q+1} \right\} \quad (29)$$

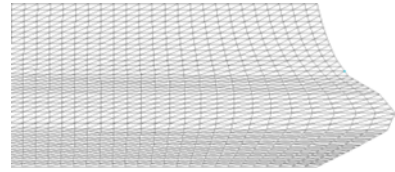


Fig. 25. New hull mesh of the modified Wigley hull by RBF method without locally refinement.

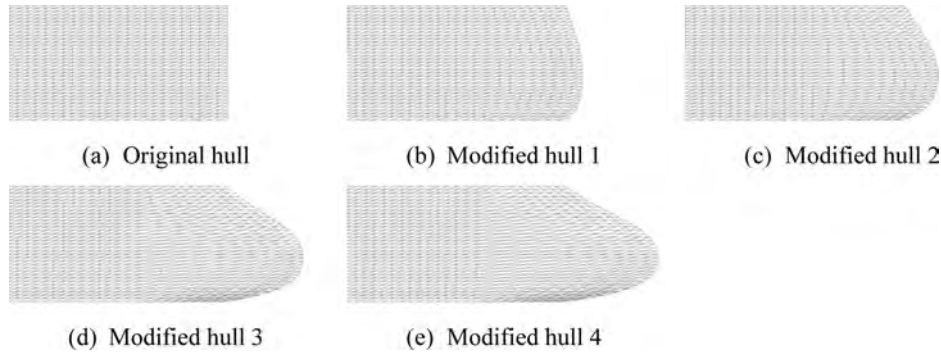


Fig. 23. Original and modified hull meshes by FFD method.

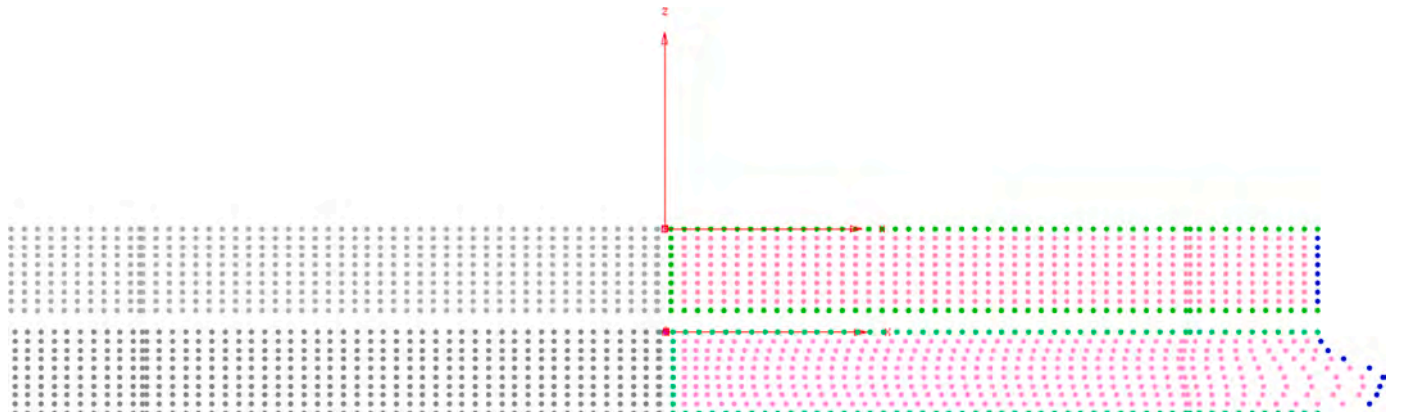


Fig. 24. Comparisons of control points of initial and modified Wigley hulls.

and we have

$$r = n + p + 1, s = m + q + 1 \quad (30)$$

The NURBS control mesh (u, v) is an approximation of the NURBS surface. The deformed mesh quality converted from the NURBS surface can be improved by properly refining the NURBS control points in the deformation region through knot-insertion algorithm. Take only one-point knot insertion as an example.

Let the NURBS curve defined on the knot vector $U = \{u_0, u_1, \dots, u_m\}$ have the following form:

$$C(u) = \frac{\sum_{i=0}^n N_{i,p}(u)\omega_i P_i}{\sum_{i=0}^n N_{i,p}(u)\omega_i} = \sum_{i=0}^n N_{i,p}(u)P_i^o, a \leq u \leq b \quad (31)$$

Now insert $\bar{u} \in [u_k, u_{k+1})$ into knot vector U to form a new knot vector \bar{U} , namely:

$$\bar{U} = \left\{ \bar{u}_0 = u_0, \dots, \bar{u}_k = u_k, \bar{u}_{k+1} = u, \bar{u}_{k+2} = u_{k+1}, \dots, \bar{u}_{m+1} = u_m \right\} \quad (32)$$

Assume that the original NURBS curve can be represented by a new knot vector \bar{U} and new NURBS control points Q_i^o , and we have

$$C(u) = \sum_{i=0}^{n+1} \bar{N}_{i,p}(u)Q_i^o, a \leq u \leq b \quad (33)$$

where $\{\bar{N}_{i,p}\}$ is a known basis function defined on a knot vector \bar{U} . The so-called knot-insertion algorithm is the process in determining Q_i^o , in order to guarantee the new NURBS curve remain unchanged from the original in terms of geometry and parameterization. The simplest way is to select values of u with the number of $(n+2)$ and substitute them into Eq. (33), and we can get

$$\sum_{i=0}^n N_{i,p}(u)P_i^o = \sum_{i=0}^{n+1} \bar{N}_{i,p}(u)Q_i^o \quad (34)$$

After mathematical derivation, the following relation can be obtained

$$Q_i^o = \alpha_i P_i^o + (1 - \alpha_i) P_{i-1}^o \quad (35)$$

where α satisfies

$$\alpha_i = \begin{cases} 1, & i \leq k - p \\ \frac{\bar{u} - u_i}{u_{i+p} - u_i}, & k - p + 1 \leq i \leq k \\ 0, & i \geq k + 1 \end{cases} \quad (36)$$

In practical application, it may be necessary to insert multiple NURBS control points (knots) in either u or v direction for NURBS surface at once, which can be implemented in a similar way as above.

Fig. 26 shows the initial Wigley hull's NURBS surface control points, while Fig. 27 shows the Wigley hull's NURBS surface control points after refinement (in main view).

After refinement, we can generate longitudinal profile of the bulbous bow. Shown in Fig. 28, blue points are the moveable points moving in x direction; green points are the fixed points which are considered in the RBF equation and located at the mid-ship station, waterline, and baseline; pink points are the dependent points whose displacement can be calculated by Eq. (2); black points, however, are the fixed points at the aft part of the ship which are not considered in the RBF equation.



Fig. 26. Initial NURBS control points of Wigley hull.

Then, generate a proper breadth of the bulbous bow, and the different types of points are shown in Fig. 29.

Finally, we can obtain the new hull by transforming the new NURBS surface to the discrete mesh and the main view of the mesh at the bow part is shown in Fig. 30, and 3-D view of the bulbous generation is also shown in Fig. 31.

4.2. Design variables

In optimization case 2, we select 7 design variables, including the four in optimization case 1 to globally change the hull by shifting method at the fore and aft parts and the other three are to change the shape of the bulbous bow by altering the two control points (P_1 and P_2) shown in Fig. 32.

The optimization design variables (dimensionless) are shown in Table 6.

Generally, there are several levels/methods to apply constraint conditions in hull form optimization designs.

First of all, the most direct and simplest constraint, as shown in the two optimization problems above, is to limit the range of geometric parameters (design variables) according to the corresponding hull form deformation methods. In this way, for surrogate-based hull form optimization, it only needs to conduct the design of experiment in a regular design space (i.e., hypercube) of the design variables. For example, OLHS or Sobol method can be used for sampling. After establishing the surrogate model, intelligent optimization algorithms, such as GA and PSO, can be finally used to solve the optimization problem, which is essentially an optimization problem containing only the maximum and minimum constraints of design variables.

Furthermore, if other constraints, such as relative changes in the wet surface area or the displacement of the hull, are needed during the optimization process, there are mainly two kinds of methods to impose for surrogate-based hull form optimization. Firstly, according to the sampling result of the design of experiment, each new sample hull can be obtained by the specified hull form deformation methods, such as FFD and RBF, and the relative changes of each new hull's wet surface area or displacement to the original hull can be calculated then, to see whether the maximum relative changes in the samples meet the constraint conditions. If the maximum relative change of the wet surface area is less than 1%, for instance, then it is considered that all new deformed hulls in the design space basically meet the requirements. Of course, after the optimal hull is obtained by the optimization algorithm, further verification of the optimal hull is needed to ensure that it truly meets the constraint conditions. On the contrary, if the maximum relative change does not meet the constraint conditions, the value range of the design variables can be adjusted.

Of course, the restriction method given above is relatively rough. As a matter of fact, for optimization problems with various constraints, the type of constraint conditions is not only the minimum or maximum value of each design variable, but also complex constraints on multiple design variables. For instance, hull geometric constraints, or even constraints on some aspect of seakeeping and maneuverability, can be given directly as constraints in the optimization algorithm by empirical formulas, or numerical simulation that the performance index should also be established as surrogate models to represent the approximate relationship between the design variables and the performance index. In other words, the surrogate models of each constraint condition, as a set of inequality constraint conditions, are finally applied to the solution of optimization problems with constraints.

More generally, in order to obtain the optimal hull form with more

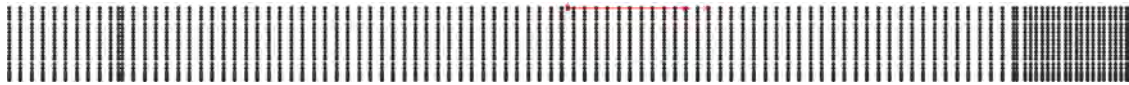


Fig. 27. Refined NURBS control points of Wigley hull.

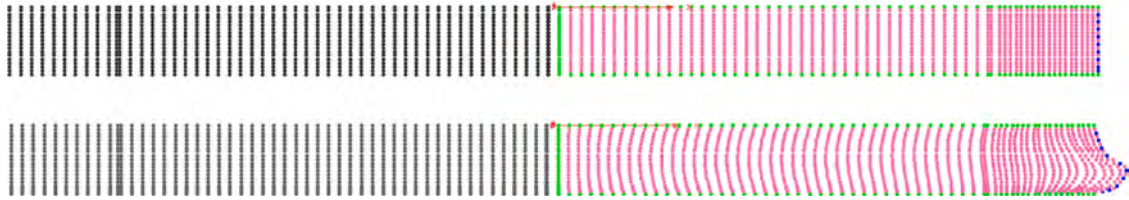


Fig. 28. Comparison of refined control points of initial and x-direction modified Wigley hulls.

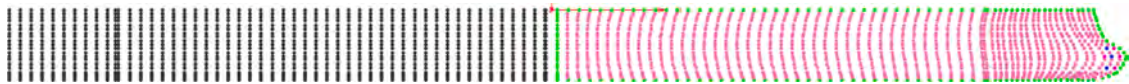


Fig. 29. Refined control points for modifying Wigley hull in y-direction.

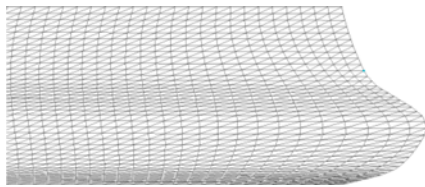


Fig. 30. New hull mesh of the modified Wigley hull by RBF method with locally refinement.



Fig. 31. 3-D view of the generation of a bulbous by RBF method.

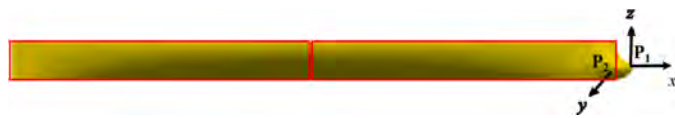


Fig. 32. Two shifting regions and moveable control points of modified Wigley hull in case 2.

Table 6
Optimization design variables in case 2.

No.	Method	Point/Region	Design Variables	Range
1	RBF	P ₁ -x	x	[0.515,0.545]
2		P ₁ -z	z	[-0.049,-0.0344]
3		P ₂ -y	y	[0.005,0.021]
4	Shifting	Region 1 (fore part)	α_1	[-0.02,0.02]
5			α_2	[0.2,0.3]
6		Region 2	α_3	[-0.02,0.02]
7		(aft part)	α_4	[-0.3,-0.2]

excellent comprehensive performances, such as resistance and sea-keeping, the multi-objective optimization algorithms like NSGA-II, can also be directly adopted to obtain a series of optimal hull forms based on Pareto front, and further select the optimal hulls according to the actual needs (such as the importance of different performance indicators).

In this case, we firstly use the OLHS method to generate 280 sample points for 280 new hull forms which are uniformly distributed in the design space, and then calculate their wave-making resistance coefficient at $Fr = 0.3$.

4.3. Optimization results and analysis

After doing the hydrodynamic evaluations of the new hull forms, the Kriging surrogate model can be constructed. Through leave-one-out cross validation, we can see the accuracy of the constructed Kriging model in Fig. 33 and the mean square error is 2.391×10^{-10} .

Finally, we use genetic algorithm with the parameters given in case 1

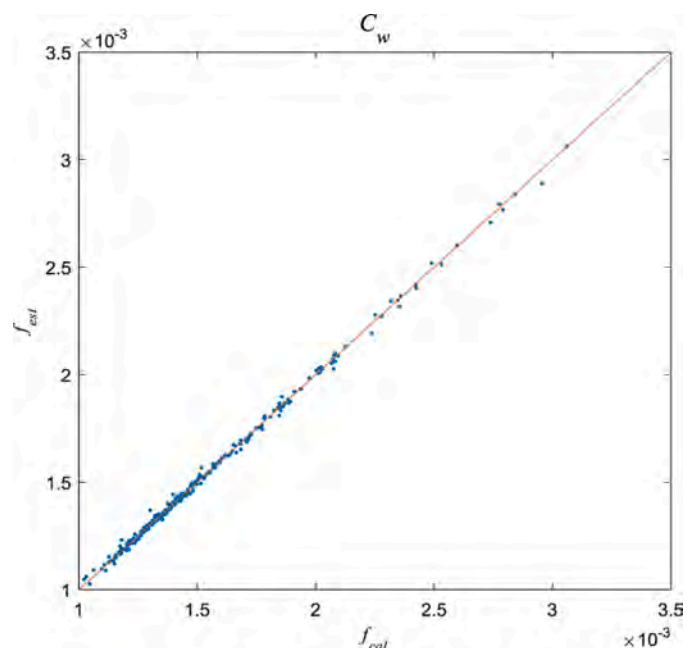


Fig. 33. Cross validation of Kriging surrogate model in case 2.

to get the optimization results. The convergence process of GA is shown in Fig. 34, the comparison of the initial and optimal hulls with its design variable values is shown in Table 7, and the hull line comparisons are shown in Fig. 35.

Totally speaking, we can see that the hull is a bit thinner than the initial one, but a relatively large bulbous bow can be seen, which is the biggest difference compared with Fig. 19. Furthermore, their free surface wave elevation comparison evaluated by NMSHIP-SJTU is shown in Fig. 36.

It can also be observed from Fig. 36 that the peaks and troughs of bow and stern diverging waves, and the stern transverse wave are all decreased due to the shifting of the cross sections and the generation of the bulbous bow. Compared with the optimal hull in case 1, the optimal one in this case has a smaller wave-making resistance coefficient, and with the generation of the bulbous bow, the phase shifting of the wave systems are more obvious, which result in more decline of the amplitudes of the peaks and troughs.

In order to do further verification like case 1, the calm-water drags of the initial and optimal hulls are calculated by naoe-FOAM-SJTU, and their free surface wave elevation comparison evaluated by naoe-FOAM-SJTU can be seen in Fig. 37.

This result given by naoe-FOAM-SJTU not only guarantees the reliability of the optimal hull in case 2, but also indicates that the NMSHIP-SJTU solver can predict the wave-making resistance (or the wave elevation) in calm water with relatively high fidelity and much less time once again.

Similar to case 1, the calm-water drag coefficients of the initial and optimal hulls calculated by the NM-based solver and RANS-based solver are listed in Table 8.

Seen from Table 8, for optimization case 2, the optimal hull has an increase of the wet surface area due to the generation of the bulbous bow, and the frictional drag coefficient C_f has a 4.8% increase. However, the pressure drag coefficient C_p has a more obvious decrease, reaching 37.9%, which is relatively close to the 47.0% decrease of the wave-making drag coefficient C_w obtained by the potential flow solver. As a result, the total drag coefficient C_t has a 11.7% decrease, indicating that the optimization results given above are effective and reliable, and the optimal hull with a generated bulbous bow can have a better resistance performance than that of the optimal hull without a bulbous bow.

Last but not the least, it is vital to discuss the CPU times needed to obtain the wave-making drag coefficient by NMSHIP-SJTU solver and total drag coefficient by naoe-FOAM-SJTU.

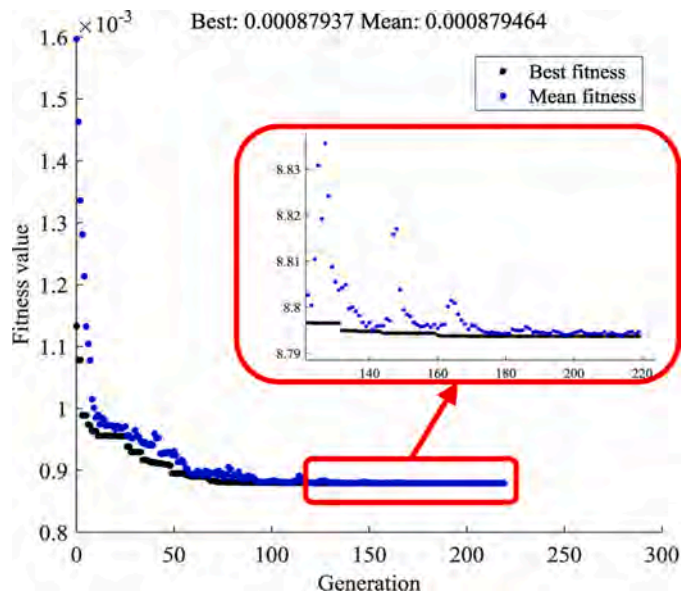


Fig. 34. Convergence of GA in case 2.

Table 7

Comparison of the design variables of initial and optimal hulls in case 2.

No.	Method	Design Variables	Initial Value	Optimal Value
1	RBF	x	0.53	0.542
2		z	-0.0417	-0.043
3		y	0.013	0.010
4	Shifting	α_1	0	0.019
5		α_2	0	0.200
6		α_3	0	0.019
7		α_4	0	-0.200

The NMSHIP-SJTU solver is run on PC, and the calculation information for a single hull is listed:

- (i) CPU information: Intel(R) i7-4790 K @ 2.00 GHz;
- (ii) grid number: hull panel about 3500; free-surface panel about 133,000;
- (iii) iteration: approximately 40 CPU seconds by 1 processor per hull panel velocity potential iteration;
- (iv) free-surface calculation: approximately 300 CPU seconds;
- (v) total CPU time: approximately 700 CPU seconds;

The naoe-FOAM-SJTU solver is implemented on High Performance Computing (HPC) cluster. For the calm-water total drag calculation of a single hull, the calculation information is listed:

- (i) CPU information: Intel(R) Xeon Gold 5120 @ 2.20 GHz;
- (ii) grid number: about 1070,000;
- (iii) iteration: approximately 4 CPU seconds by 56 processors per time step $\Delta t = 0.001$ s;
- (iv) total CPU time: approximately 175,000 CPU seconds;

For the calm-water drag evaluation of one ship hull, according to the grid quantity and calculation time given above, it is not difficult to see that the time needed to solve the wave drag coefficient by using NM theory (700 s) is only 1/250 of that needed to solve the total drag coefficient by using the viscous flow solver (175,000 s). It is enough to prove that the use of potential flow theory has superiority for the resistance performance optimization of hull form.

Furthermore, for surrogate-based optimization, if the number of design variables is relatively high, in order to ensure that the fidelity of the established surrogate model for the ship performance indicator reaches a high level, more sample points are needed when doing the design of experiment.

Therefore, during the calm-water resistance optimization for medium- or high-speed ships in the early design stage, since a large number of the new hulls need to be evaluated, when using the potential flow theory, the total time of the whole optimization process can be sharply decreased compared with that using the viscous flow theory. Meanwhile, the potential-flow based drag optimization can seize the trend of optimization of drag well, and the obtained optimal hull can demonstrate the reliability of the optimization results, from the perspectives of both total drag coefficient and the free surface wave elevation field.

Although the two applications are both single-objective optimization design problems, the surrogate-based hull form optimization procedure given here has the extension ability to multi-objective optimization problems in order to realize its potential in comprehensive hydrodynamic performance hull form optimization design problems.

As a matter of fact, the hull form optimization process based on the surrogate model can not only be used for a single condition or a single performance indicator, but also for multiple conditions or multiple performance indicators, such as multi-objective calm-water drag optimization considering different speeds, comprehensive performances of hull form optimization considering resistance and seakeeping, etc. Therefore, the proposed procedure can be extended to multi-objective optimization. However, for multi-objective hull form optimization

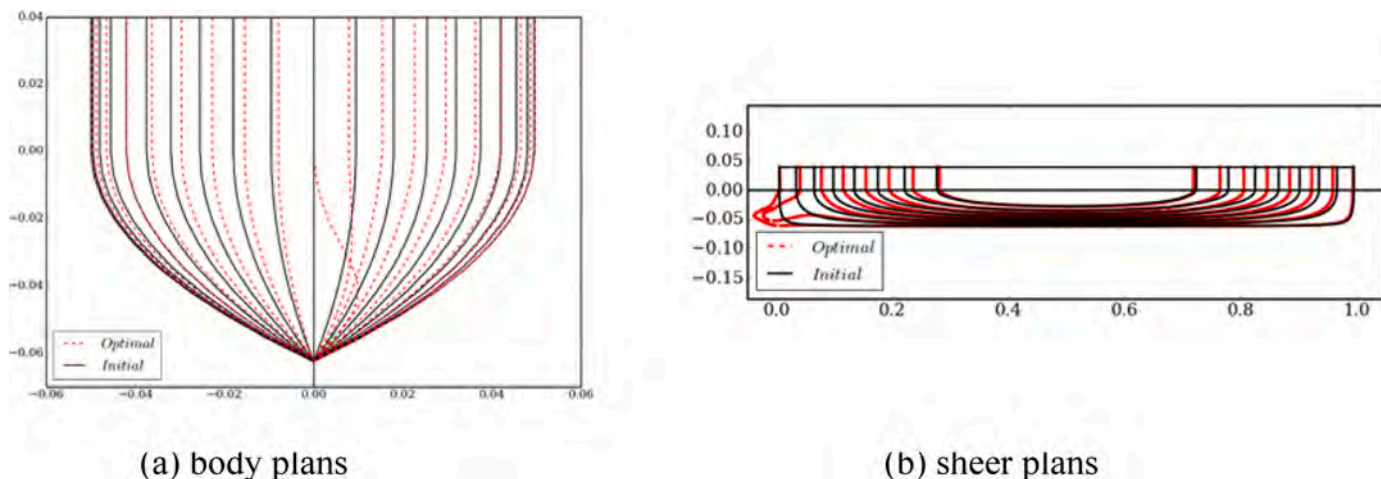


Fig. 35. Hull line comparisons of the two hulls in case 2.

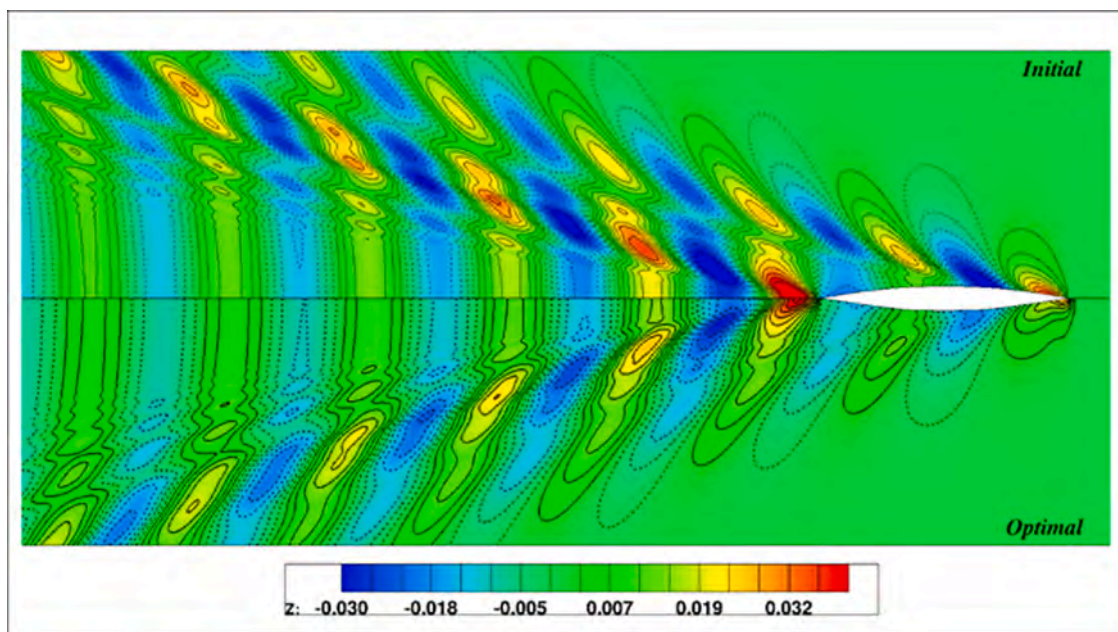


Fig. 36. Wave elevation comparison of the two hulls in case 2 by NMSHIP-SJTU (Unit: m).

problems, since more than one surrogate model of the objective functions should be established before the optimization solution, there may be relatively many working conditions or performance indicators to be calculated, resulting in more calculation costs. Meanwhile, it is difficult to obtain a single optimal hull form due to the possible contradiction between different indicators. Therefore, multi-objective optimization algorithms, such as Non-dominated Sorting Genetic Algorithm II (NSGA-II) and Multi-Objective Particle Swarm Optimization (MOPSO), can be adopted to obtain a series of optimal hulls based on Pareto front for further selection.

5. Conclusions

The Wigley hull is adopted as original hull form whose objective function is the wave-making resistance coefficient at $Fr = 0.3$ by a numerical optimization tool, OPTSHIP-SJTU, which has huge potentials in the optimization of ship hydrodynamic performances.

Verification and validation of the NMSHIP-SJTU is implemented with systematic 3 sets of grids is done in comparing the drag coefficients. Furthermore, the wave height along the hull are also compared with the

experimental results.

During the optimization progress, Optimal Latin Hypercube Sampling method is used to generate new hull forms, and Kriging model is used as the surrogate model, which has relatively high fidelity. Furthermore, the use of Neumann-Michell theory as the prediction method is proved to be very effective compared with the RANS-based naoe-FOAM-SJTU solver.

In the process of bulbous bow generation, proper deformation method should be used so that the quality of new hull meshes can be ensured, and the knot-insertion procedure for the NURBS surface is also introduced.

Two optimization cases are given for comparing the optimization effect with or without generating a bulbous bow. Even when we do not generate a bulbous bow, the optimal hull will have a relatively big decrease of the wave drag coefficient, shown in case 1. However, favorable interference of the wave systems conducted by the generated bulbous bow can help reduce the wave drag coefficient to a greater extent, as shown in case 2.

Last but not the least, the way in which constraints are handled has been discussed especially for the hull form optimization problems.

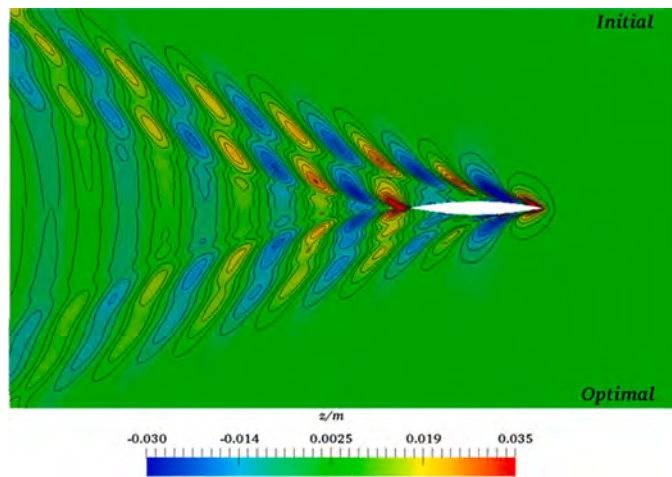


Fig. 37. Wave elevation comparison of the two hulls in case 2 by naoe-FOAM-SJTU (Unit: m).

Table 8

Comparison of the drag coefficients of initial and optimal hulls in case 2.

	C_w (NM)	C_p (RANS)	C_f (RANS)	C_t (RANS)
Initial	1.66×10^{-3}	1.81×10^{-3}	2.87×10^{-3}	4.68×10^{-3}
Optimal	0.88×10^{-3}	1.12×10^{-3}	3.01×10^{-3}	4.13×10^{-3}
Decrease percent	47.0%	37.9%	-4.8%	11.7%

Actually, there are several levels/methods to apply constraint conditions in hull form optimization designs. In parallel, a study on hull form optimization problems with more complex constraints is being done.

Declaration of Competing Interest

The authors declare that they have no known competing financial interests or personal relationships that could have appeared to influence the work reported in this paper.

Acknowledgments

This work is supported by the National Key Research and Development Program of China (2019YFB1704200 and 2019YFC0312400), National Natural Science Foundation of China (51879159), to which the authors are most grateful.

References

Bates, S., Sienz, J., Toropov, V., 2004. Formulation of the optimal latin hypercube design of experiments using a permutation genetic algorithm. In: Proc 45th AIAA/ASME/ASCE/AHS/ASC Structures, Structural Dynamics & Materials Conf, No. AIAA-2004-2011.

Berberović, E., Van, H.N., Jakirlić, S., Roisman, I., Tropea, C., 2009. Drop impact onto a liquid layer of finite thickness: dynamics of the cavity evolution. *Phys. Rev. E* 79 (3), 36306.

Campana, E.F., Peri, D., Tahara, Y., Stern, F., 2006. Shape optimization in ship hydrodynamics using computational fluid dynamics. *Comput. Method Appl. M.* 196 (1), 634–651.

Deb, K., Agrawal, R.B., 1995. Simulated binary crossover for continuous search space. *Complex Syst.* 9, 115–148.

Diez, M., Campana, E.F., Stern, F., 2015. Design-space dimensionality reduction in shape optimization by Karhunen–Loève expansion. *Comput. Method Appl. M.* 283, 1525–1544.

Kim, H., Yang, C., Chun, H.H., 2009. Hydrodynamic optimization of a modern container ship using variable fidelity models. In: Proc 19th Int Offshore and Polar Eng Conf. ISOPE.

Kim, H., Yang, C., Jeong, S., Noblesse, F., 2011. Hull form design exploration based on response surface method. In: Proc 21st Int Offshore and Polar Eng Conf. ISOPE, pp. 816–827.

Li, S.Z., Ni, Q.J., Zhao, F., Liu, H., 2013. Multi-objective design optimization of stern lines for full-formed ship. *Shipbuilding China* 2013 (3), 1–10.

Liu, X.W., Wan, D.C., 2017. Numerical analysis of wave interference among the demihulls of the high-speed quadamarans. *Shipbuilding China* 58 (1), 140–151.

Liu, X.W., Wang, J.K., Wan, D.C., 2018. Hull form optimization design of KCS at full speed range based on resistance performance in calm water. In: Proc 28th Int Offshore and Polar Eng Conf. ISOPE, pp. 626–632.

Menter, F.R., Kuntz, M., Langtry, R., 2003. Ten years of industrial experience with the SST turbulence model. *Turbul. Heat Mass Transf.* 4, 625–632.

Noblesse, F., Huang, F.X., Yang, C., 2013. The Neumann-Michell theory of ship waves. *J. Eng. Math.* 79 (1), 51–71.

OpenFOAM, 2016. The OpenFOAM Foundation. URL <http://openfoam.org/>.

Peri, D., 2016. Robust design optimization for the refit of a cargo ship using real seagoing data. *Ocean Eng.* 123, 103–115.

Peri, D., Rossetti, M., Campana, E.F., 2001. Design optimization of ship hulls via CFD techniques. *J. Ship Res.* 45 (2), 140–149.

Sederberg, T.W., Parry, S.R., 1986. Free-form deformation of solid geometric primitives. *Comput. Graph.* 20 (4), 151–160.

Shen, Z.R., Cao, H.J., Ye, H.X., Wan, D.C., 2012. The Manual of CFD Solver For Ship and Ocean Engineering flows: naoe-FOAM-SJTU. No. 2012SR118110. Shanghai Jiao Tong University.

Shen, Z.R., Wan, D.C., 2013. RANS computations of added resistance and motions of a ship in head waves. *Int. J. Offshore Polar Eng.* 23 (4), 264–271.

Sobol, I., 1979. On the systematic search in a hypercube. *SIAM J. Numer. Anal.* 16 (5), 790–793.

Sykulski, A.M., Adams, N.M., Jennings, N.R., 2011. On-line adaptation of exploration in the one-armed bandit with covariates problem. In: Proc 9th Int Conf on Machine Learning and Application. IEEE, pp. 459–464.

Tahara, Y., Peri, D., Campana, E.F., Stern, F., 2008. Single and multi-objective design optimization of a fast multihull ship: numerical and experimental results. In: Proc 27th Symposium on Naval Hydrodyn. Korea, pp. 25–33.

Tezdogan, T., Zhang, S.L., Yigit, K.D., Liu, W.D., Xu, L.P., Lai, Y.Y., Kurt, R.E., Djatmiko, E.B., Incecik, A., 2018. An investigation into fishing boat optimisation using a hybrid algorithm. *Ocean Eng.* 167, 204–220.

Wang, J.H., Zhao, W.W., Wan, D.C., 2019. Development of naoe-FOAM-SJTU solver based on OpenFOAM for marine hydrodynamics. *J. Hydrodyn.* 31 (1), 1–20.

Wilson, R.V., Stern, F., Coleman, H.W., Paterson, E.G., 2001. Comprehensive approach to verification and validation of CFD Simulations-Part 2: application for rans simulation of a cargo/container ship. *J. Fluid Eng.* 123 (4), 803–810.

Wendland, H., 1995. Piecewise polynomial, positive definite and compactly supported radial functions of minimal degree. *Adv. Comput. Math.* 4 (1), 389–396.

Wu, J.W., Liu, X.Y., Zhao, M., Wan, D.C., 2017. Neumann-Michell theory-based multi-objective optimization of hull form for a naval surface combatant. *Appl. Ocean Res.* 63, 129–141.

Yang, C., Huang, F.X., 2016. An overview of simulation-based hydrodynamic design of ship hull forms. *J. Hydrodyn.* 28 (6), 947–960.

Yang, C., Huang, F.X., Noblesse, F., 2013. Practical evaluation of the drag of a ship for design and optimization. *J. Hydrodyn.* 25 (5), 645–654.

Zha, R.S., Ye, H.X., Shen, Z.R., Wan, D.C., 2014. Numerical computations of resistance of high speed catamaran in calm water. *J. Hydrodyn.* 26 (6), 930–938.

Zhang, B.J., Ma, K., Ji, Z.S., 2009. The optimization of the hull form with the minimum wave making resistance based on Rankine source method. *J. Hydrodyn.* 21 (2), 277–284.

Zhang, C.L., He, J.Y., Ma, C., Wan, D.C., 2015. Validation of the Neumann-Michell theory for two catamarans. In: Proc 25th Int Offshore and Polar Eng Conf. ISOPE.

Zhang, X.S., Wang, J.H., Wan, D.C., 2020. Numerical techniques for coupling hydrodynamic problems in ship and ocean engineering. *J. Hydrodyn.* 32 (2), 212–233.

Zhao, M.S., Zhao, W.W., Wan, D.C., 2020a. Numerical simulations of propeller cavitation flows based on OpenFOAM. *J. Hydrodyn.* 32 (6), 1071–1079.

Zhao, W.W., Wang, J.H., Wan, D.C., 2020b. Vortex identification methods in marine hydrodynamics. *J. Hydrodyn.* 32 (2), 286–295.

Zhuang, Y., Wan, D.C., 2021. Parametric study of a new HOS-CFD coupling method. *J. Hydrodyn.* 33 (1), 43–54.